Iridium-Nickel Nanoparticle-Based Aerogels for Oxygen Evolution Reaction

Seongeun Park,[a] Nikolai Utsch,[a] Marcelo Carmo,[a,d,#] Meital Shviro[a,ϕ,*] and Detlef Stolten[b,c]

[a] Institute of Energy and Climate Research, Electrochemical Process Engineering (IEK-14)
Forschungszentrum Jülich GmbH, 52425 Jülich, Germany
[b] Institute of Energy and Climate Research, Techno-economic Systems Analysis (IEK-3)
Forschungszentrum Jülich GmbH, 52425 Jülich, Germany
[c] Chair for Fuel Cells, RWTH Aachen University, Germany
[d] Mechanical and Materials Engineering, Queen's University, Kingston, ON, K7L 3N6, Canada
[#] Present address: Nel Hydrogen, 10 Technology Drive, Wallingford, CT, 06492, United States
[ϕ] Present address: Chemistry and Nanoscience Center, National Renewable Energy Laboratory (NREL),
Golden, CO, 80401, United States

ABSTRACT: Iridium is considered the state-of-the-art electrocatalyst for the oxygen evolution reaction (OER) in acidic media due to its considerably high activity and stability, yet it is a raw material that is expensive and rare. Here we present a synthesis of a bimetallic hollow aerogel structure based on iridium and nickel prepared by a very simple and environmentally friendly method. Our electrocatalyst was evaluated for OER in a single electrolysis cell and it showed an improvement in electrocatalytic performance over time, reaching the current density of commercial IrO_2 after 500 hours of stability test, despite half the catalyst loading. Our innovative synthesis approach provides the flexibility to tailor and improve the aerogel structures for other electrochemical devices as well, for example, photoelectrolysis, sensors, and more. In addition, we believe that this study can lead to a better understanding of the fundamental behavior of bimetallic electrocatalysts consisting of mixed compositions with transition metals.

Keywords: iridium, aerogel, bimetallic electrocatalysts, oxygen evolution reaction, electrolysis, PEM

---

1. Introduction

Water splitting is attracting a lot of attention as an environmentally friendly alternative to produce green hydrogen, which is considered one of the most important energy sources for the future.[1–3] Proton exchange membrane (PEM) water electrolysis possesses clear advantages such as high current density, compact stack design, wide load range, etc.[4–6] However, its components must be highly corrosion resistant since it operates in conditions that combine high electrode potential and strong acidic media. In the last years, the cost of many stack components such as bipolar plates or membranes has been significantly reduced.[7,8] The electrocatalyst for hydrogen evolution reaction (HER) has been diversified and highly developed,[9,10] but the electrocatalyst for the oxygen evolution reaction (OER) is still iridium. Unfortunately, iridium is scarce in reserves, with a limited annual production, causing its price to be extremely volatile and unpredictable for the giga/terawatt scale deployment of PEM electrolyzers.[11,12] These circumstances urge us to improve the utilization of iridium.[13]

Toward an efficient and economic electrocatalyst, iridium has been researched in various ways as other materials. Decreasing particle size is the most representative way to develop catalysts by increasing the specific surface area.[14,15] Bizzotto et al. synthesized extremely small iridium nanoparticles which were approximately 1.6 nm of size and proved that size control can induce the efficient utilization of iridium.[14] Fabrication of hollow nanostructures is also a common strategy due to its effective surface exposure.[16–18] In general, transition metals are utilized in the design of hollow structures, which expects not only improved catalytic activity via d-band engineering but also economic effect by saving the usage of noble metals.[19–21] Kwon et al. reported Co-doped IrCu hollow octahedral nanocages that were synthesized through the removal of Cu component using acid, which showed boosted electrocatalytic activity and durability.[21] Another approach is introduction of supporting materials, which can assist the catalytic activity of iridium with high conductivity and preserve iridium stably.[22–24] Hartig-Weiss et al. fabricated iridium nanoparticles supported on antimony-doped tin oxide that enabled the reduction of precious metal 75 times.[23] However, most of these reported catalyst alternatives still some bottlenecks for the single cell level, for instance, limits in fabrication process for large scale, easy agglomeration or loss of catalysts, possible dissolution of additional materials that will disturb the system eventually, etc.

After considering these drawbacks in the development of electrocatalysts, aerogel remains as a very attractive structure to be applied as electrocatalysts. Aerogel has been used in various applications such as sensing[25–27], adsorbents[28,29], insulator[30], etc.[31–33] Recently it is on the spotlight as catalysts due to its attractive properties.[34–39] Firstly, aerogel is self-standing three-dimensional (3D) structure, which has no need to be supported by other materials. It can prevent cell degradation possibly caused by the dissolution of additional materials and instead use the volume more efficiently. It also provides extremely large specific surface area with high porosity. Due to the physical properties, the density of aerogels is highly low in most cases, which leads us to expect a cost-saving effect in cell development. Liu et al. introduced PtAg nanotubular aerogels that indicated 19-folds improved mass activity by comparison with commercial Pt black for formic acid oxidation.[40] Du et al. showed that their Au-based multimetallic aerogels presented highly active performance in the evaluation for hydrogen evolution reaction and oxygen reduction reaction.[41]

We present here Ir-Ni aerogel synthesized at room temperature by an environmentally friendly process based on DI water. The Ir-Ni aerogel had a well-crosslinked chain-like 3D structure with an average thickness of 30 nm. It is composed of hollow nanoparticles uniformly mixed with iridium and nickel, which was achieved by in-situ leaching effect as a control of reaction rate. The Ir-Ni aerogel was evaluated as an electrocatalyst for OER in an acidic electrolyte. When tested in a 25 cm^2 electrolysis cell, the Ir-Ni aerogel showed improved catalytic performance as the cycles continued, originating from the electrochemically leached nickel during the measurement. In addition, in the 500-hour of stability test, the Ir-Ni aerogel catalyst showed an evolving process that the leaching of nickel from the structure acts as a prolonged activation, which presented comparable electrocatalytic activity with half loading when compared to commercial IrO_2.

2. Experimental section

Materials

Dihydrogen hexachloroiridate(IV) hydrate (H_2IrCl_6, 99 %, Alfa Aesar), Nickel (II) chloride ($NiCl_2$, Alfa Aesar), DI water, Sodium borohydride ($NaBH_4$, MERCK) were used without additional purification.

Synthesis of Ir-Ni Aerogels: 0.05M of H_2IrCl_6 (7.5 ml) and $NiCl_2$ (2.5 ml) were added in 900 ml of DI water. After enough stirring, 50 mmol of $NaBH_4$ that dissolved in 100 ml of DI water was rapidly added under stirring. After 2 min, the solution was closed and stayed for approximately 2 days at ambient temperature. The synthesized Ir-Ni aerogels were washed in DI water for several times and dried under vacuum condition.

Morphological, Structural and Elemental Characterization. Scanning electron microscopy (SEM) was conducted on Hitachi SU8000 at an accelerating voltage of 15 kV. Scanning transmission electron microscopy (STEM) and energy dispersive X-ray (EDX) spectroscopy investigations were conducted using an FEI (Thermo Fisher Scientific) Titan 80–200 electron microscope that utilized a probe corrector (CEOS) and an HAADF detector.[42] To achieve "Z-contrast" conditions, a probe semi-angle of 25 mrad was used with the detector having a 70 mrad inner collection angle. For the EDX elemental mapping, Ir L and Ni K peaks were utilized. X-ray diffractions (XRD) were measured in D8 DISCOVER (Bruker) using a Cu Ka source and LYNXEYE_XE_T as detector. X-Ray photoelectron spectroscopy (XPS) was performed on a PHI 5000 Versaprobe II instrument with a monochromatic Al K α X-ray source. The powder samples were pressed into Indium foil which was fixed with clamps on a stainless-steel sample holder. The core level spectra were recorded with a pass energy of 23.5 eV, 0.1 eV energy step and a spot size of 200 μm. An electron flood gun and an Ar+ ion gun were used for charge compensation. The spectra were charge corrected by setting the binding energy of the main C 1s component to 285 eV. Inductively coupled plasma mass spectrometry (ICP-MS) was measured in Agilent 7900 to determine the weight ratio of iridium and nickel in materials.

Electrochemical Measurements. Electrochemical measurements were conducted using a typical three-electrode setup with a reversible hydrogen electrode (RHE) as the reference electrode and a Pt mesh rod as the counter electrode. The working electrode was a glassy-carbon electrode (GC) (diameter: 5 mm, area: 0.196 cm^2). For this working electrode, the ink was prepared by mixing the 3.5 mg of catalysts with 0.7 mg of Vulcan X-72 in DI water (6.0 ml), ethanol (4.0 ml), and 5 % of Nafion (40 ul). The mixture was sonicated for 30 min to form homogeneous ink. In this case, 10 ul of well-dispersed ink was dropped onto the GC and dried naturally at room temperature. The loading amount of catalyst on the GC was calculated as 17.8 ug cm^{-2}. The cell was purged with N_2 gas before starting the measurements. Cyclic voltammetry was carried out between +0.4 V to +1.4 V with a scan rate of 50 mV s^{-1}. Linear sweep voltammetry was recorded from +0.4 V to +1.7 V with a scan rate of 5 mV s^{-1} at O_2 saturated. The masses of catalysts were determined as the iridium amounts among the coated catalyst materials onto the GC. The overpotentials were calculated using the geometric surface area of GC (0.196 cm^2).

MEA fabrication. Anodes were made by using a spray-coating device (ExactaCoat, Sono-Tel). The stable dispersion was prepared with enough sonication and stirring by mixing catalyst material, Nafion ionomer (Ion Power), DI water and n-propanol (Merck), which was sprayed on a decal sheet. Cathodes used here were made with a doctor-blade (Coatmaster 510, Erichsen GmbH & Co. KG). The ink for cathode was prepared as a mixture of catalyst (60 % Pt/C, PK catalyst), Nafion ionomer, DI water and 2-butanol (Merck), which was dispersed by a dispersion device (Ultraturrax, IKA) and ultrasonication finger (Sonopuls HD3400, Bandelin). The cathode possessed 20 wt% of Nafion, while 11 wt% of Nafion was chosen for the anode. The catalyst layers (25 cm^2) were transferred onto the Nafion membrane (N117, Chemours) by hot-pressing at 130 °C with using a joining time of 3 min at 1.6 $kN\cdot cm^{-2}$.

Single cell testing. As porous transport layer (PTL) on the anode, a both-sided iridium sputtered Titanium fiber mesh (Bekipor® ST Titanium Grade 1) was used. The thickness of sputtered iridium layer was 20 nm, and its amount was 0.05 – 0.1 $mg_{Ir}\cdot cm^{-2}$ per side. After assembly of single cell, it was tested using an ETS E100 electrolyzer test station (Greenlight Innovation). The operation temperature was set to 80 °C while a water flow of 50 $mL\cdot min^{-1}$ was maintained using atmospheric pressure. The first 2 hours in the beginning were used for preliminary conditioning and equilibration. Afterwards, the cell was operated for 30 min at a current density of 0.2 $mA\cdot cm^{-2}$, followed by an increased current density to 1.0 $mA\cdot cm^{-2}$, which was held for another 30 min. The last step for the activation was a continual operation step with a 1.7 V of cell potential for 8 hours. For the performance test, potentiostatic testing was used and each measurement points were held for 5 min until a maximum voltage of 2.0 V was reached. For each test, forward and backward scans were performed. The current densities were determined by the geometric surface area (25 cm^2).

Potentiostatic electrochemical impedance spectroscopy (PEIS) measurements. The cell was disconnected from the test station and connected to a potentiostat (HCP1005 Biologic). The sinus amplitude was set to 10 mV and the frequency range from 10 kHz to 100 mHz was chosen for each measurement.

3. Results and discussion

3.1 Catalyst characterization

The Ir-Ni aerogel was synthesized via the sol-gel method[43,44] which is explained in more detail in the experimental section. Briefly, H_2IrCl_6 and $NiCl_2$ were dissolved in DI water. After 10 min, $NaBH_4$ solution was rapidly injected into the metal precursors solution with vigorous stirring to reduce both metal precursors into nanoparticles (Supporting Video S1). The mechanism for the preparation of Ir-Ni aerogel can be seen in a schematic illustration (Figure 1A); (1) Initially, the metal salts in the solution were quickly reduced with a sufficient amount of $NaBH_4$. The reduced Ir-Ni nanoparticles shown as a dark black colored solution are suspended with cations (Na^+) and anions (BH_4^-) from the excessively provided reducing agent. The BH_4^- bound to the surface of the Ir-Ni nanoparticles decomposes to BO_2^- with the formation of H_2 bubbles in the water. (2) Since the BO_2^- has a lower affinity than BH_4^- to a metallic surface, it is easily removed from the surface, exposing the surface of the Ir-Ni nanoparticles.[45] (3) Due to the detachment of BO_2^- and H_2 bubbles, the nanoparticles experience sufficient collisions, causing them to attract each other via surface interactions such as high surface energy and van der Waals force. As a result, the suspended nanoparticles spontaneously combine and (4) form the 3D structure on the bottom with time, which is confirmed by the transparency of the solution and the sinking product on the bottom of the bottle (Figure S1). Interestingly, the formed structure was reproducible even when separated for a time. The deposited Ir-Ni aerogel was destroyed by vigorous shaking but reconstructed soon by their surface interaction (Supporting Video S2).

Figure 1B shows the photographs of the as-prepared Ir-Ni aerogel, which exhibit typical 3D architectures in the macroscale. Scanning electron microscopy (SEM) was used to investigate the morphology of the as-prepared Ir-Ni aerogel (Figure 1C). It discloses the hierarchical morphology with the 3D networking structure. The detailed morphology of Ir-Ni aerogel was observed by high-angle annular dark-field (HAADF) scanning transmission electron microscopy (STEM) images (Figure 1D). The Ir-Ni nanoparticles were found to have a size of 27.8 ± 6.2 nm and observed as hollow structures. Elemental mapping by energy-dispersive X-ray (EDX) confirmed that the Ir-Ni aerogel consists of hollow nanoparticles uniformly mixed with 60 at% iridium and 40 at% nickel (Figure 1E). Here we explain that the formation of the hollow nanostructures was induced during the synthesis and could be controlled by the reaction rate.

As reported in the literature, iridium requires higher energy to be reduced, which induces the reduction rate of iridium relatively slower than other elements.[17,21,46] Accordingly, it rarely forms by itself at the beginning of the reaction but prefers to be coated on the area having high surface energy from others.[47–49] That is, if we consider the kinetics between iridium and nickel when both elements react together, it is spontaneous that nickel forms the core first and the formation of the iridium shell follows, which was calculated by Wang et al. in their study using density functional theory (DFT).[50] We discovered that the Ir-Ni aerogel with core-shell nanostructure was formed in a different experimental condition when the reaction speed was increased. (Figure S2). The experiment was performed in a 100 ml flask with heating at 100 ^{o}C, which provided almost 48 times higher volume density and much more energy for the materials in the reaction. Under the reaction conditions, nickel formed the core structure (red) first due to the relatively fast reduction rate, followed by the coating of iridium (green) on the nickel surface, which completed the core-shell structure of the aerogel (Figure S2B). On the contrary, it is believed that nickel was directly leached from the structure during synthesis under the reaction conditions, resulting in the hollow nanostructure. We explain that this occurred with sufficient reaction time in the acidic environment caused by the iridium precursor. The susceptible nickel was leached out of the structure over time under acidic conditions, and the resulting vacancies were used by iridium and nickel to form the well-mixed bimetallic hollow nanoparticles by the Kirkendall effect.[51–53]

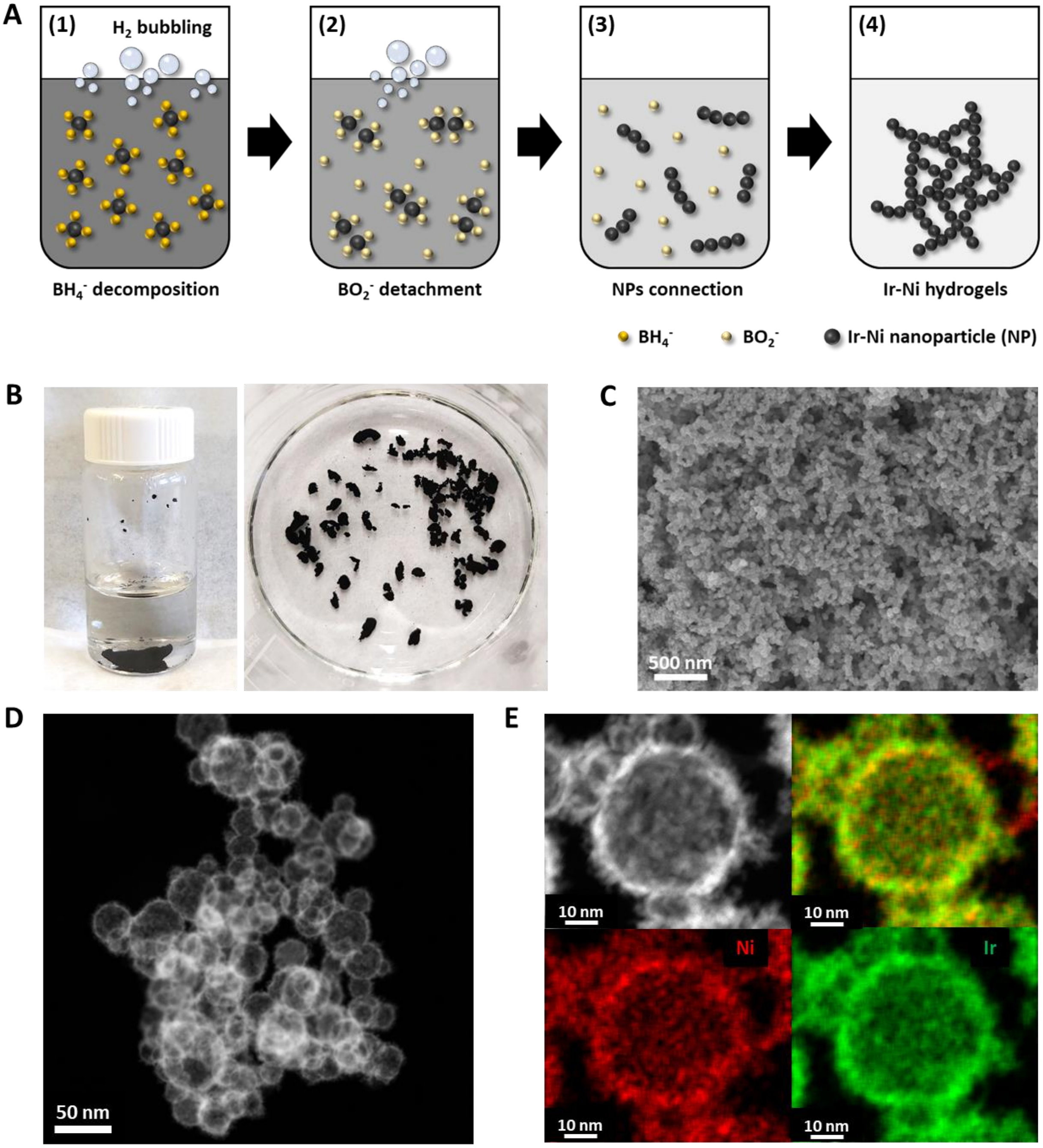

Figure 1. (A) Schematic illustration to describe the fabrication mechanism of Ir-Ni aerogel, and morphological characterization of Ir-Ni aerogel; (B) Photos after synthesis, (C) SEM image, (D) HAADF-STEM image and (E) the elemental distribution of Ni (red) and Ir (green) by EDX composition maps.

The structure of the Ir-Ni aerogel was further analyzed by X-ray diffraction (XRD), as shown in Figure 2A. The distinct peaks associated with planes (111), (200), (220), and (311) correspond to the typical facecentered cubic (FCC) crystal structure of iridium (JCPDS 06-0598). It also shows the broadened peaks that may be caused by the nanoscale structure, alloy composition with nickel, and more reasons. In particular, the peak around 45°, which has a shoulder-like peak, implies the existence of a strong (111) peak for the FCC structure of nickel (JCPDS 03-1051), which is commonly observed in alloys of iridium and nickel.[17,54] The alloy composition and crystallinity of Ir-Ni aerogel were also presented in the high-resolution TEM observation (Figure S3). The HRTEM image with the Fast Fourier transform (FFT) pattern for Ir-Ni aerogel nanoparticles reveals the Ir-Ni FCC structure by showing 2 Å of lattice distance, corresponding to the (111) planes for Ir-Ni.

The surface composition of the Ir-Ni aerogel was analyzed by X-ray photoelectron spectroscopy (XPS) and presented in Figure 2B-D. The Ir 4f region displayed in Figure 2B indicates that the Ir-Ni aerogel has metallic iridium species (Ir^0) with 85.0 at% and oxidized iridium (Ir^{x+}) with 15.0 at% on the surface, implying that the sensitive surface was already slightly oxidized in the experimental environment. The nickel spectra in the Ni $2p_{3/2}$ region showed oxidized nickel as Ni^{3+} with 80.7 at% and metallic species (Ni^0) with 19.3 at%, suggesting that the nickel has a metallic core and an oxidized shell considered as γ-NiOOH (Figure 2C).[55] Figure 2D shows the O 1s region describing the peaks for oxide (-O), hydroxide (-OH), and adventitious spectra normally associated with adsorbed water (H_2O) with proportions of 12.9 at%, 72.2 at%, and 14.9 at%, respectively. The oxide peak is believed to be the result of oxidized iridium and oxidized nickel. In the case of the hydroxide peak, it is interpreted that more than one factor would be involved in it, when considered that γ-NiOOH possesses a lower intensity of hydroxide species than the one for its oxide species.[56,57] We explain that the leached nickel may also contribute to the hydroxide species, since it has been reported that the hydroxyl group can be generated on the iridium surface when nickel is leached out from the structure.[58] Overall, the Ir-Ni aerogel surface consists of metallic iridium and oxidized nickel (nickel oxyhydroxide).

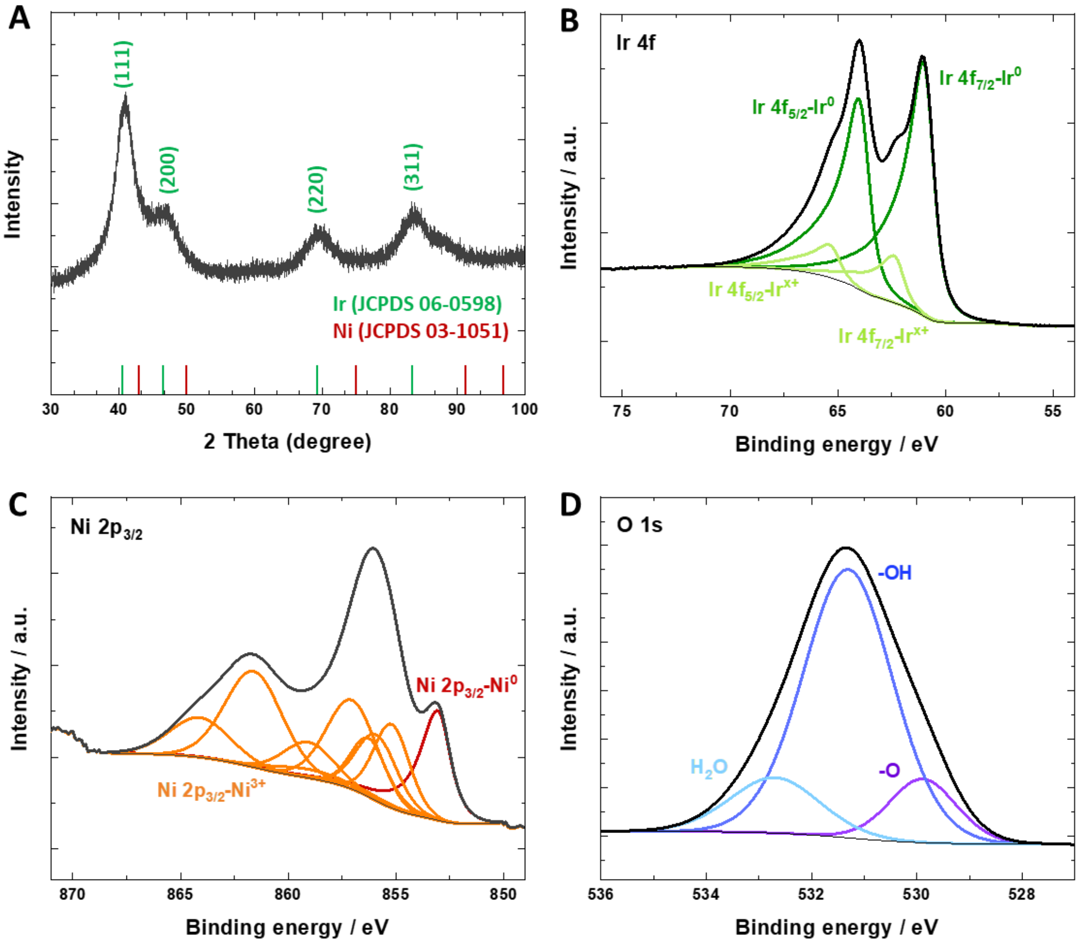

Figure 2. (A) XRD patterns and X-ray photoelectron spectra of Ir-Ni aerogels in the (B) Ir 4f, (C) Ni $2p_{3/2}$, (D) O 1s regions.

3.2 Electrochemical measurements

The Ir-Ni aerogel was investigated as an electrocatalyst for OER in an acidic electrolyte in a three-electrode system. Before evaluating the electrocatalytic performance, the electrochemically active surface area (ECSA) of Ir-Ni aerogel was measured in comparison with commercial IrO_2 from Alfa Aesar. ECSA was obtained by taking the total anodic charges from the cyclic voltammetry (CV) profiles after double-layer corrected in the potential range of 0.4 V to 1.25 V (vs. RHE) using a conversion factor of 440 $\mu C \cdot cm^{-2}$.[59] The determined ECSA value for IrO_2 was 20.4 $m^2 \cdot g_{Ir}^{-1}$, on the contrary, Ir-Ni aerogel exhibited 15.5 $m^2 \cdot g_{Ir}^{-1}$. Brunauer-Emmett-Teller (BET) was analyzed in comparison with the ECSA results. From the N_2 adsorption/desorption measurements, the surface area was 28.9 ± 1.2 $m^2 \cdot g^{-1}$ for Ir-Ni aerogel, which is low giving the morphology but doubles the value of ECSA. We attribute this discrepancy between measurements and lack of reliability to the deficiency of access to the interior of the porous aerogel structure in current evaluation methods for ECSA. The ECSA calculation applied here is commonly used and known as an appropriate method for oxidized surface, however, it still has some considerably limited assumptions, for example, the ideally flat surface of electrocatalysts or monometallic composition. Moreover, as evidenced by other literature showing unclear aspects for ECSA determination, it is still a challenge to obtain a trustworthy result for iridium-based catalysts.[60–62]

To evaluate catalytic activity, cyclic voltammetry was performed between 0.4 V and 1.4 V (vs. RHE) at a scan rate of 500 $mV·s^{-1}$ for 45 cycles, followed by 50 $mV·s^{-1}$ of lower scan rate to observe redox peaks. After CV sweeping, OER activity was evaluated using linear sweep voltammetry (LSV) from 0.4 V to 1.7 V (vs. RHE) at a scan rate of 5 $mV·s^{-1}$ in an oxygen saturated electrolyte. Figure 3A shows the initial OER polarization curve for Ir-Ni aerogel and the commercial IrO_2 from Alfa Aesar, which presented the superior activity of Ir-Ni aerogel to commercial IrO_2 with 7.8 % lower overpotential. The iridium mass activities at 1.51 V for each electrocatalyst were also indicated in Figure 3B. Considering the testing condition such as catalyst loading, the activity of Ir-Ni aerogel showed the improved activity when compared to the other reported catalytic activity for Ir-based materials (Table S1). To evaluate the stability of electrocatalysts, each electrocatalyst was cycled from 1.1 V to 1.6 V at 100 $mV·s^{-1}$ 1,000 times. As a result, the overpotential for the Ir-Ni aerogels were increased by 4.9 % after the stability test, however, commercial IrO_2 showed relatively higher degradation with 6.1 % (Figure 3C). To find out the kinetic behavior of the electrocatalysts, we analyzed their Tafel slopes for oxygen evolution derived from their polarization curves (Figure 3D). Before the stability test, the Ir-Ni aerogel showed 53.6 $mV·dec^{-1}$ of Tafel slope, indicating that its rate-determining step is mainly focused on the formation of the chemically active hydroxide group on the electrocatalyst surface.[63,64] After the stability test, the Ir-Ni aerogel even showed a 48.0 $mV·dec^{-1}$ of lower slope than before, which is interpreted that nickel in the aerogel structure is electrochemically leached during cycling that favored the formation of an active hydroxide group, inducing the faster reaction. In contrast, the commercial IrO_2 started with 64.2 $mV·dec^{-1}$ but showed an increased Tafel slope (70.5 $mV·dec^{-1}$) after the stability test. The Tafel slopes were in the range typically reported for IrO_2 catalysts, which implies that the rate-determining step is highly involved in the first electron transfer step.[23,24,64–66] However, the reaction rate is presented to be slower after the stability test.

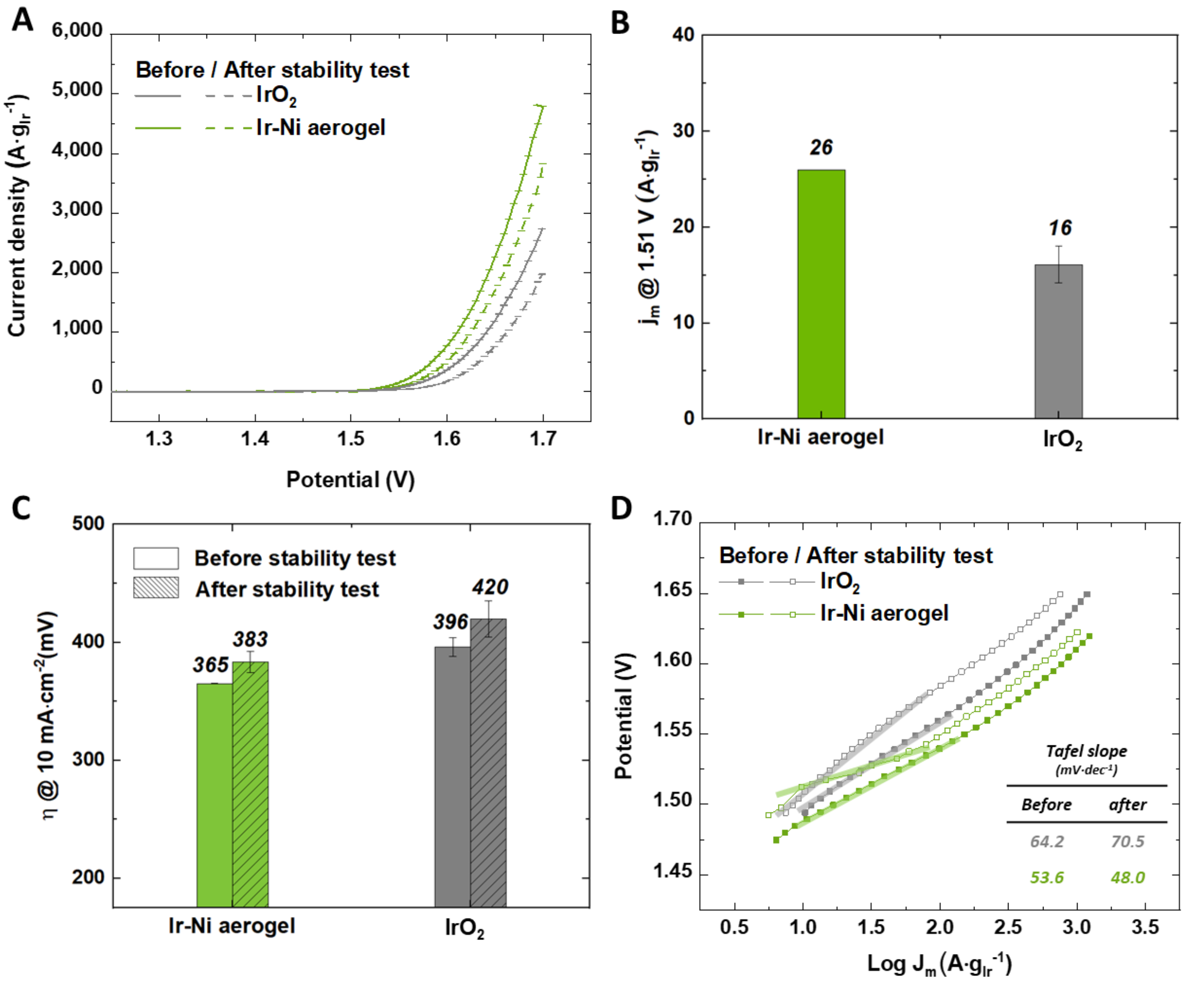

Figure 3. Electrochemical measurements of Ir-Ni aerogel by comparison with commercial IrO_2 (Alfa Aesar). (A) OER polarization curves measured in 0.5 M H_2SO_4 before and after the stability test; (B) Ir mass activities at 1.51 V (vs. RHE); (C) bar graphs displaying the overpotentials to drive 10 mA·cm^{-2} and (D) Tafel plots before and after the stability test.

Afterwards, the Ir-Ni aerogel was evaluated in a single cell in comparison to commercial IrO_2 (Figure 4). Both catalysts were laminated on Nafion N117 membranes and tested at ambient pressure, 80 °C, in 25 cm^2 cells. The stability of our aerogel catalyst was evaluated under industry-relevant conditions at 2.0 V for 500 hours (Table S2). Figure 4 shows the change in current density of Ir-Ni aerogel with a loading of 1.0 mg$_{Ir}$·cm^{-2}, in comparison to commercial IrO_2 with a loading of 2.2 mg$_{Ir}$·cm^{-2}. The commercial IrO_2 initially presented the current density of 2.46 A·cm^{-2}, but it was degraded to 2.35 A·cm^{-2} over time, which is a typical performance decay that can be observed in the literature.[62,67–70] It can be originated from various circumstances for IrO_2 catalysts, for example, dissolution into electrolyte, detachment from electrode, particle agglomeration, and more.[66,70–75] In contrast to this behavior, the Ir-Ni aerogel exhibited 2.07 A·cm^{-2} at the beginning, but it continuously increased and reached 2.27 A·cm^{-2} after 500 hours. The electrocatalytic activity improved continuously during the measurement, and we assume that this behavior of the Ir-Ni aerogel is caused by the electrochemically leached nickel during the measurements. As previously reported in the literature, when nickel is leached out from catalyst structure, it remains an active hydroxide group on the surface, which improves the OER activity.[54,58,60,76] Accordingly, dissolution of the nickel here is assumed to act as "activation" of the electrodes responsible to increase its electrochemical surface area. This was confirmed in additional tests by continuous CV cycles (Figure S4). To investigate the effect of the "activation process" achieved by electrochemically leached nickel, the polarization curves of the Ir-Ni aerogel electrode were observed as the cycles progressed to reach 2.0 V for 70 cycles, which showed that the performance continued to increase as the cycles continued, but with gradual saturation. The effect of electrochemically leached nickel is also confirmed by electrochemical impedance spectroscopy (EIS) Nyquist plots for the Ir-Ni aerogel before and after the 500 hours of long-term stability test (Figure S5). Before testing, it showed a curve that was speculated as additional resistance related with nickel occurred at the double-layer on the surface such as diffusion phenomena but nearly disappeared after the test. After testing, the high-frequency resistance (HFR) decreased by 0.03 Ω·cm^2, implying that the contact efficiency for electrocatalytic reaction could be improved during the long-term stability test, which might be affected by the removed nickel disturbing the contact between the catalyst and porous transport layer. Furthermore, it achieved better reaction kinetics with lower charge transfer resistance after testing. Meanwhile, in the polarization performed after the 500 hours of stability test, it was confirmed that the 'activation' of Ir-Ni aerogel was still continued (Figure S6). From the 2.27 A·cm^{-2} after 500 hours, it continued to improve and reached 2.31 A·cm^{-2} after the test. This explains that the stability test worked as an evolving process for the Ir-Ni aerogel, not the deteriorating condition for other catalysts. We also point out here that our Ir-Ni aerogel implemented the comparable performance to IrO_2, the state-of-the-art electrocatalyst for OER even with lower than half of its loading. The electrochemically leached nickel from the Ir-Ni aerogel structure during the measurements functioned as longer activation rather than degradation, which enhanced the electrocatalytic activity as much as the performance of commercial IrO_2 with half loading that can bring the cost reduction of PEM water electrolyzer eventually.

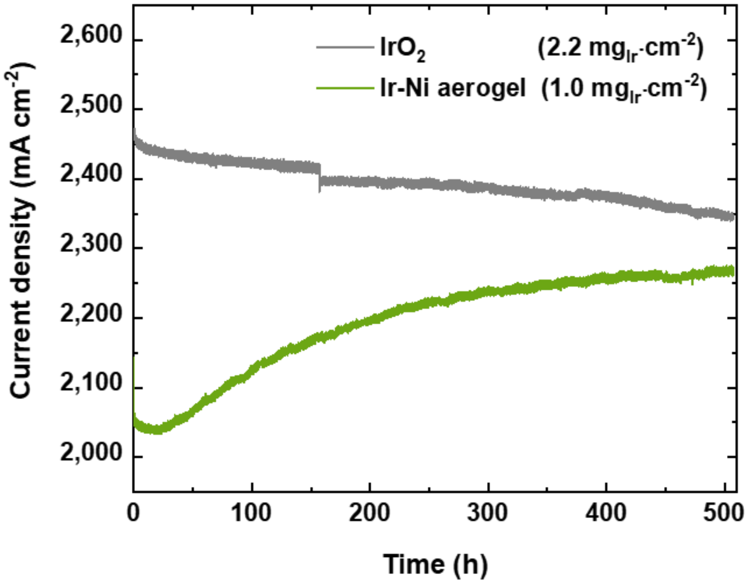

Figure 4. Current density at 2.0 V for 500 hours as long-term stability test by comparison with commercial IrO_2 (Alfa Aesar).

To determine the effects of the stability test, the catalyst coated membrane (CCM) were analyzed after the test and compared to pristine CCM. The morphological change on the anode side was observed by SEM, indicating that agglomeration or coarsening was hardly found (Figure S7). The corresponding backscattering image confirmed the well-retained porous structure of the aerogel. At the same time, EDX confirmed that only 4 at% of the nickel remained, suggesting that the rest of the nickel was leached out during the electrochemical measurements. Investigation of the cross-sections revealed that the coated layers for the cathode and anode were slightly detached from the membrane overall, speculated that the layers were destroyed when the cell was disassembled. It might also be affected during the sample preparation procedure for SEM. Nonetheless, the electrode layers themselves generally showed stable layers with no wrinkled areas (Figure S8). Based on the highlighted blue color and the magnified images, it was confirmed that the anode was hardly damaged, and the coated layer was well preserved after the test (Figure S8C-F).

XRD measurements were performed for the anode side to compare the crystallinity before and after testing (Figure S9). Before testing, the anode showed a similar result with the synthesized Ir-Ni aerogel XRD pattern, which fits the metallic iridium FCC structure (JCPDS 06-0598) alloyed with nickel. However, after the stability test, the pattern showed a clear change that the intensities of metallic iridium peaks were decreased overall and the peaks possibly indicating oxidized iridium were emerged, which implies that the oxidation of iridium in anode was remarkably proceeded.[77–79]

To determine the change in the chemical and oxidation state of the anode surface before and after the test, XPS analysis was performed (Figure S10). Unfortunately, the specific nickel spectra could not be obtained due to the strong intensity of the fluoride peak contained in the Nafion, which is almost positioned with the nickel.[80] The iridium spectra before and after the test showed a clear change (Figure S10A). Before the test, the anode possessed only metallic iridium species located on the 60.9 eV and 63.9 eV, but after the test, they completely transformed into oxidized iridium spectra indicating 61.9 eV and 64.9 eV of binding energies. It implies that the formation of oxidized iridium is placed on the surface with the majority of $3^+/4^+$ oxidation state.[81] The O 1s region also exhibited remarkable species changes (Figure S10B). It was measured to originally have a very low fraction of oxide peak (-O) of 6.0 at% and a relatively high fraction of hydroxide peak (-OH) (see 'Before testing'). The adventitious peak of 43.5 at% is thought to be the adsorbed water (H_2O) on the anode surface. After 500 hours of the test, the adsorbed water had decreased to 25.2 at%, while the oxide peak and hydroxide peak increased relatively to 9.3 at% and 65.5 at%, respectively (see 'After 500 hours'). Furthermore, a shift of hydroxide peak was also observed, speculated as the effect of leached nickel during the electrochemical measurements. Considering that most of the nickel was leached from the anode, it is interpreted that the oxide spectra are from the oxidized iridium and the hydroxide spectra are related to the formed hydroxyl group of the leached nickel, which explains the improved electrocatalytic performance during the long-term test.

"In summary, the activation mechanism is achieved by nickel that leached electrochemically from the catalyst structure. Although a proper activation step was previously performed, the nickel, which is susceptible under the test conditions, is dissolved during the test. The leached nickel leaves the functional group, which is electrochemically more efficient for OER, on the catalyst surface and possibly also increases the physical surface area. This occurs slowly over more than 500 hours while maintaining the aerogel structure, resulting in performance enhancement rather than degradation."

4. Conclusions

In summary, Ir-Ni aerogel with a bimetallic hollow nanostructure was synthesized for the first time. It was composed of uniform alloy composition of iridium and nickel and achieved as a hollow nanostructure without additional treatment via the reaction rate control during synthesis. The synthesis is environmentally friendly and conveniently scaled up. The Ir-Ni aerogel was evaluated in single electrolysis cells and compared to commercial IrO_2. In the 500-hour stability test, the Ir-Ni aerogel showed that the electrochemical performance was improved throughout the measurements, while the commercial IrO_2 was degraded due to its instability. This is explained as the ‘activation process’ for Ir-Ni aerogel originated from the electrochemically leached nickel during measurements. Even after the 500 hours of stability test, the performance of Ir-Ni aerogel enhanced and recorded 2.31 A·cm^{-2} with 1.0 mg·cm^{-2} which corresponds to half the iridium loading compared commercial IrO_2 CCM. After testing, the 3D chain-like structure of the Ir-Ni aerogel was well preserved without coarsening or agglomeration, which was easily observed in the disordered separated nanoparticles, indicating better electrocatalytic stability. With Ir-Ni aerogel, we were able to reveal the synthesis mechanism of the bimetallic hollow aerogel structure and observe the electrochemical behavior of iridium-based bimetallic materials as electrocatalysts for OER. The synthesis presented here will give flexibility to the design of the aerogel structure and expand its use in other applications by demonstrating its simplicity and proving its beneficial properties. Moreover, we believe that this study helps understanding the electrocatalytic behavior of iridium-based bimetallic nanostructures and supports strategies to use them more wisely.

ASSOCIATED CONTENT

Supporting information

The supporting information is available free of charge at https:// pubs.acs.org/

Video for showing the color change in the first 15 seconds with stirring.
Video for showing the reconstruction of Ir-Ni aerogel after breaking of connection.
Photos showing reaction, TEM images, Polarization curves, Nyquist plots, SEM images, XRD, and XPS results to compare before and after long-term testing. Table showing the operating conditions applied during the 500 hours of long-term stability test

AUTHOR INFORMATION

Corresponding Author

Meital Shviro- Institute of Energy and Climate Research, Electrochemical Process Engineering (IEK-14) Forschungszentrum Jülich GmbH, 52425 Jülich, Germany; Present address: Chemistry and Nanoscience Center, National Renewable Energy Laboratory (NREL), Golden, CO, 80401, United States; Email: meital.shviro@nrel.gov

Authors

Seongeun Park- Institute of Energy and Climate Research, Electrochemical Process Engineering (IEK-14) Forschungszentrum Jülich GmbH, 52425 Jülich, Germany

Nikolai Utsch- Institute of Energy and Climate Research, Electrochemical Process Engineering (IEK-14) Forschungszentrum Jülich GmbH, 52425 Jülich, Germany

Marcelo Carmo- Institute of Energy and Climate Research, Electrochemical Process Engineering (IEK-14) Forschungszentrum Jülich GmbH, 52425 Jülich, Germany; Mechanical and Materials Engineering, Queen's University, Kingston, ON, K7L 3N6, Canada; Present address: Nel Hydrogen, 10 Technology Drive, Wallingford, CT, 06492, United States

Detlef Stolten- Institute of Energy and Climate Research, Techno-economic Systems Analysis (IEK-3) Forschungszentrum Jülich GmbH, 52425 Jülich, Germany; Chair for Fuel Cells, RWTH Aachen University, Germany

Notes

There are no conflicts to declare.

Acknowledgements

The authors would like to thank Moritz Weber for the scientific discussion, also to Daniel Holtz, Stefanie Fischer, Andreas Everwand, Birgit Schumacher and Heinrich Hartmann for the experimental support.

Notes and references

(1) Fajrina, N.; Tahir, M. A Critical Review in Strategies to Improve Photocatalytic Water Splitting towards Hydrogen Production. *Int J Hydrogen Energy* **2019**, *44* (2), 540–577. https://doi.org/10.1016/J.IJHYDENE.2018.10.200.

(2) Wang, S.; Lu, A.; Zhong, C.-J. Hydrogen Production from Water Electrolysis: Role of Catalysts. *Nano Convergence 2021 8:1* **2021**, *8* (1), 1–23. https://doi.org/10.1186/S40580-021-00254-X.

(3) Li, X.; Zhao, L.; Yu, J.; Liu, X.; Zhang, X.; Liu, H.; Zhou, W. Water Splitting: From Electrode to Green Energy System. *Nano-Micro Letters 2020 12:1* **2020**, *12* (1), 1–29. https://doi.org/10.1007/S40820-020-00469-3.

(4) Carmo, M.; Fritz, D. L.; Mergel, J.; Stolten, D. A Comprehensive Review on PEM Water Electrolysis. *Int J Hydrogen Energy* **2013**, *38* (12), 4901–4934. https://doi.org/10.1016/j.ijhydene.2013.01.151.

(5) Shiva Kumar, S.; Himabindu, V. Hydrogen Production by PEM Water Electrolysis – A Review. *Mater Sci Energy Technol* **2019**, *2* (3), 442–454. https://doi.org/10.1016/J.MSET.2019.03.002.

(6) Liu, C.; Shviro, M.; Gago, A. S.; Zaccarine, S. F.; Bender, G.; Gazdzicki, P.; Morawietz, T.; Biswas, I.; Rasinski, M.; Everwand, A.; Schierholz, R.; Pfeilsticker, J.; Müller, M.; Lopes, P. P.; Eichel, R.; Pivovar, B.; Pylypenko, S.; Friedrich, K. A.; Lehnert, W.; Carmo, M. Exploring the Interface of Skin-Layered Titanium Fibers for Electrochemical Water Splitting. *Adv Energy Mater* **2021**, 2002926. https://doi.org/10.1002/aenm.202002926.

(7) Mayyas, A.; Ruth, M.; Pivovar, B.; Bender, G.; Wipke, K. Manufacturing Cost Analysis for Proton Exchange Membrane Water Electrolyzers. **2019**.

(8) Babic, U.; Suermann, M.; Büchi, F. N.; Gubler, L.; Schmidt, T. J. Review-Identifying Critical Gaps for Polymer Electrolyte Water Electrolysis Development. *J Electrochem Soc* **2017**, *164* (4), F387–F399. https://doi.org/10.3929/ETHZ-B-000190719.

(9) Lin, Z.; Wang, Z.; Shen, S.; Chen, Y.; Du, Z.; Tao, W.; Xu, A.; Ye, X.; Zhong, W.; Feng, S. One-Step Method to Achieve Multiple Decorations on Lamellar MoS2 to Synergistically Enhance the Electrocatalytic HER Performance. *J Alloys Compd* **2020**, *834*, 155217. https://doi.org/10.1016/J.JALLCOM.2020.155217.

(10) Lin, Z.; Wang, C.; Wang, Z.; Liu, Q.; Le, C.; Lin, B.; Chen, S. The Role of Conductivity and Phase Structure in Enhancing Catalytic Activity of CoSe for Hydrogen Evolution Reaction. *Electrochim Acta* **2019**, *294*, 142–147. https://doi.org/10.1016/J.ELECTACTA.2018.10.082.

(11) Vesborg, P. C. K.; Jaramillo, T. F. Addressing the Terawatt Challenge: Scalability in the Supply of Chemical Elements for Renewable Energy. *RSC Adv* **2012**, *2* (21), 7933–7947. https://doi.org/10.1039/C2RA20839C.

(12) Mudd, G. M. Key Trends in the Resource Sustainability of Platinum Group Elements. *Ore Geol Rev* **2012**, *46*, 106–117. https://doi.org/10.1016/j.oregeorev.2012.02.005.

(13) Bernt, M.; Hartig-Weiß, A.; Tovini, M. F.; El-Sayed, H. A.; Schramm, C.; Schröter, J.; Gebauer, C.; Gasteiger, H. A. Current Challenges in Catalyst Development for PEM Water Electrolyzers. *Chemie Ingenieur Technik* **2020**, *92* (1–2), 31–39. https://doi.org/10.1002/cite.201900101.

(14) Bizzotto, F.; Quinson, J.; Zana, A.; Kirkensgaard, J. J. K.; Dworzak, A.; Oezaslan, M.; Arenz, M. Ir Nanoparticles with Ultrahigh Dispersion as Oxygen Evolution Reaction (OER) Catalysts: Synthesis and Activity Benchmarking. *Catal Sci Technol* **2019**, *9* (22), 6345–6356. https://doi.org/10.1039/C9CY01728C.

(15) Lettenmeier, P.; Wang, L.; Golla-Schindler, U.; Gazdzicki, P.; Cañas, N. A.; Handl, M.; Hiesgen, R.; Hosseiny, S. S.; Gago, A. S.; Friedrich, K. A. Nanosized IrO x -Ir Catalyst with Relevant Activity for Anodes of Proton Exchange Membrane Electrolysis Produced by a Cost-Effective Procedure. *Angewandte Chemie* **2016**, *128* (2), 752–756. https://doi.org/10.1002/ange.201507626.

(16) Park, J.; Kwon, T.; Kim, J.; Jin, H.; Kim, H. Y.; Kim, B.; Joo, S. H.; Lee, K. Hollow Nanoparticles as Emerging Electrocatalysts for Renewable Energy Conversion Reactions. *Chem Soc Rev* **2018**, *47* (22), 8173–8202. https://doi.org/10.1039/C8CS00336J.

(17) Park, S.; Shviro, M.; Hartmann, H.; Besmehn, A.; Mayer, J.; Stolten, D.; Carmo, M. Nickel Structures as a Template Strategy to Create Shaped Iridium Electrocatalysts for Electrochemical

Water Splitting. *ACS Appl Mater Interfaces* **2021**, *13*, 13576–13585. https://doi.org/10.1021/acsami.0c23026.

(18) Prieto, G.; Tüysüz, H.; Duyckaerts, N.; Knossalla, J.; Wang, G.-H.; Schüth, F. Hollow Nano- and Microstructures as Catalysts. *Chem Rev* **2016**, *116* (22), 14056–14119. https://doi.org/10.1021/ACS.CHEMREV.6B00374.

(19) Feng, J.; Lv, F.; Zhang, W.; Li, P.; Wang, K.; Yang, C.; Wang, B.; Yang, Y.; Zhou, J.; Lin, F.; Wang, G.-C.; Guo, S. Iridium-Based Multimetallic Porous Hollow Nanocrystals for Efficient Overall-Water-Splitting Catalysis. *Advanced Materials* **2017**, *29* (47), 1703798. https://doi.org/10.1002/adma.201703798.

(20) Park, J.; Choi, S.; Oh, A.; Jin, H.; Joo, J.; Baik, H.; Lee, K. Hemi-Core@frame AuCu@IrNi Nanocrystals as Active and Durable Bifunctional Catalysts for the Water Splitting Reaction in Acidic Media. *Nanoscale Horiz* **2019**, *4* (3), 727–734. https://doi.org/10.1039/C8NH00520F.

(21) Kwon, T.; Hwang, H.; Sa, Y. J.; Park, J.; Baik, H.; Joo, S. H.; Lee, K. Cobalt Assisted Synthesis of IrCu Hollow Octahedral Nanocages as Highly Active Electrocatalysts toward Oxygen Evolution Reaction. *Adv Funct Mater* **2017**, *27* (7), 1604688. https://doi.org/10.1002/adfm.201604688.

(22) Pham, C. Van; Bühler, M.; Knöppel, J.; Bierling, M.; Seeberger, D.; Escalera-López, D.; Mayrhofer, K. J. J.; Cherevko, S.; Thiele, S. IrO2 Coated TiO2 Core-Shell Microparticles Advance Performance of Low Loading Proton Exchange Membrane Water Electrolyzers. *Appl Catal B* **2020**, *269* (February), 118762. https://doi.org/10.1016/j.apcatb.2020.118762.

(23) Hartig-Weiss, A.; Miller, M.; Beyer, H.; Schmitt, A.; Siebel, A.; Freiberg, A. T. S.; Gasteiger, H. A.; El-Sayed, H. A. Iridium Oxide Catalyst Supported on Antimony-Doped Tin Oxide for High Oxygen Evolution Reaction Activity in Acidic Media. *ACS Appl Nano Mater* **2020**. https://doi.org/10.1021/acsanm.9b02230.

(24) Li, G.; Li, K.; Yang, L.; Chang, J.; Ma, R.; Wu, Z.; Ge, J.; Liu, C.; Xing, W. Boosted Performance of Ir Species by Employing TiN as the Support toward Oxygen Evolution Reaction. *ACS Appl Mater Interfaces* **2018**, *10* (44), 38117–38124. https://doi.org/10.1021/acsami.8b14172.

(25) Zhuo, H.; Hu, Y.; Chen, Z.; Peng, X.; Liu, L.; Luo, Q.; Yi, J.; Liu, C.; Zhong, L. A Carbon Aerogel with Super Mechanical and Sensing Performances for Wearable Piezoresistive Sensors. *J Mater Chem A Mater* **2019**, *7* (14), 8092–8100. https://doi.org/10.1039/c9ta00596j.

(26) Yang, J.; Li, Y.; Zheng, Y.; Xu, Y.; Zheng, Z.; Chen, X.; Liu, W. Versatile Aerogels for Sensors. *Small* **2019**, *15* (41), 1902826. https://doi.org/10.1002/smll.201902826.

(27) Li, Q.; Li, Q.; Chen, D.; Chen, D.; Miao, J.; Miao, J.; Lin, S.; Lin, S.; Yu, Z.; Yu, Z.; Han, Y.; Yang, Z.; Zhi, X.; Cui, D.; Cui, D.; An, Z. Ag-Modified 3D Reduced Graphene Oxide Aerogel-Based Sensor

with an Embedded Microheater for a Fast Response and High-Sensitive Detection of NO2. *ACS Appl Mater Interfaces* **2020**, *12* (22), 25243–25252. https://doi.org/10.1021/acsami.9b22098.

(28) Lu, Y.; Zhang, B.; Liu, S.; Yin, L.; Gong, W.; Gao, J.; Zhang, Z.; Ning, W. Pd/SiO2 Aerogel Composite Adsorbents with High Desulfurization Performance. *J Chem Eng Data* **2020**, *65* (2), 923–934. https://doi.org/10.1021/acs.jced.9b01122.

(29) Kong, Y.; Jiang, G.; Fan, M.; Shen, X.; Cui, S.; Russell, A. G. A New Aerogel Based CO2 Adsorbent Developed Using a Simple Sol-Gel Method along with Supercritical Drying. *Chemical Communications* **2014**, *50* (81), 12158–12161. https://doi.org/10.1039/c4cc06424k.

(30) Xu, X.; Zhang, Q.; Hao, M.; Hu, Y.; Lin, Z.; Peng, L.; Wang, T.; Ren, X.; Wang, C.; Zhao, Z.; Wan, C.; Fei, H.; Wang, L.; Zhu, J.; Sun, H.; Chen, W.; Du, T.; Deng, B.; Cheng, G. J.; Shakir, I.; Dames, C.; Fisher, T. S.; Zhang, X.; Li, H.; Huang, Y.; Duan, X. Double-Negative-Index Ceramic Aerogels for Thermal Superinsulation. *Science (1979)* **2019**, *363* (6428), 723–727. https://doi.org/10.1126/science.aav7304.

(31) Yang, J.; Zhang, E.; Li, X.; Zhang, Y.; Qu, J.; Yu, Z. Z. Cellulose/Graphene Aerogel Supported Phase Change Composites with High Thermal Conductivity and Good Shape Stability for Thermal Energy Storage. *Carbon N Y* **2016**, *98*, 50–57. https://doi.org/10.1016/j.carbon.2015.10.082.

(32) Sun, H.; Mei, L.; Liang, J.; Zhao, Z.; Lee, C.; Fei, H.; Ding, M.; Lau, J.; Li, M.; Wang, C.; Xu, X.; Hao, G.; Papandrea, B.; Shakir, I.; Dunn, B.; Huang, Y.; Duan, X. Three-Dimensional Holey-Graphene/Niobia Composite Architectures for Ultrahigh-Rate Energy Storage. *Science (1979)* **2017**, *356* (6338), 599–604. https://doi.org/10.1126/science.aam5852.

(33) Shi, K.; Huang, X.; Sun, B.; Wu, Z.; He, J.; Jiang, P. Cellulose/BaTiO 3 Aerogel Paper Based Flexible Piezoelectric Nanogenerators and the Electric Coupling with Triboelectricity. *Nano Energy* **2019**, *57*, 450–458. https://doi.org/10.1016/j.nanoen.2018.12.076.

(34) Du, R.; Wang, J.; Wang, Y.; Hübner, R.; Fan, X.; Senkovska, I.; Hu, Y.; Kaskel, S.; Eychmüller, A. Unveiling Reductant Chemistry in Fabricating Noble Metal Aerogels for Superior Oxygen Evolution and Ethanol Oxidation. https://doi.org/10.1038/s41467-020-15391-w.

(35) Fu, S.; Zhu, C.; Song, J.; Engelhard, M. H.; He, Y.; Du, D.; Wang, C.; Lin, Y. Three-Dimensional PtNi Hollow Nanochains as an Enhanced Electrocatalyst for the Oxygen Reduction Reaction †. **2016**. https://doi.org/10.1039/c6ta01801g.

(36) Liu, W.; Haubold, D.; Rutkowski, B.; Oschatz, M.; Hübner, R.; Werheid, M.; Ziegler, C.; Sonntag, L.; Liu, S.; Zheng, Z.; Herrmann, A. K.; Geiger, D.; Terlan, B.; Gemming, T.; Borchardt, L.; Kaskel, S.; Czyrska-Filemonowicz, A.; Eychmüller, A. Self-Supporting Hierarchical Porous PtAg Alloy Nanotubular Aerogels as Highly Active and Durable Electrocatalysts. *Chemistry of Materials* **2016**, *28* (18), 6477–6483. https://doi.org/10.1021/acs.chemmater.6b01394.

(37) Fu, S.; Zhu, C.; Du, D.; Lin, Y. Enhanced Electrocatalytic Activities of PtCuCoNi Three-Dimensional Nanoporous Quaternary Alloys for Oxygen Reduction and Methanol Oxidation Reactions. *ACS Appl Mater Interfaces* **2016**, *8* (9), 6110–6116. https://doi.org/10.1021/acsami.6b00424.

(38) Du, R.; Jin, W.; Hübner, R.; Zhou, L.; Hu, Y.; Eychmüller, A. Engineering Multimetallic Aerogels for PH-Universal HER and ORR Electrocatalysis. *Adv Energy Mater* **2020**, *10* (12), 1903857. https://doi.org/10.1002/aenm.201903857.

(39) Shafaei Douk, A.; Saravani, H. Porous 3D Inorganic Superstructure of Pd–Ir Aerogel as Advanced Support-Less Anode Electrocatalyst toward Ethanol Oxidation. *ACS Omega* **2020**, acsomega.0c01661. https://doi.org/10.1021/acsomega.0c01661.

(40) Liu, W.; Haubold, D.; Rutkowski, B.; Oschatz, M.; Hübner, R.; Werheid, M.; Ziegler, C.; Sonntag, L.; Liu, S.; Zheng, Z.; Herrmann, A. K.; Geiger, D.; Terlan, B.; Gemming, T.; Borchardt, L.; Kaskel, S.; Czyrska-Filemonowicz, A.; Eychmüller, A. Self-Supporting Hierarchical Porous PtAg Alloy Nanotubular Aerogels as Highly Active and Durable Electrocatalysts. *Chemistry of Materials* **2016**, *28* (18), 6477–6483. https://doi.org/10.1021/acs.chemmater.6b01394.

(41) Du, R.; Jin, W.; Hübner, R.; Zhou, L.; Hu, Y.; Eychmüller, A. Engineering Multimetallic Aerogels for PH-Universal HER and ORR Electrocatalysis. *Adv Energy Mater* **2020**, *10* (12), 1903857. https://doi.org/10.1002/aenm.201903857.

(42) Kovács, A.; Schierholz, R.; Tillmann, K. FEI Titan G2 80-200 CREWLEY. *Journal of large-scale research facilities JLSRF* **2016**, *2* (0), A43. https://doi.org/10.17815/jlsrf-2-68.

(43) Liu, W.; Herrmann, A.-K.; Bigall, N. C.; Rodriguez, P.; Wen, D.; Oezaslan, M.; Schmidt, T. J.; Gaponik, N.; Eychmüller, A. Noble Metal Aerogels—Synthesis, Characterization, and Application as Electrocatalysts. *Acc Chem Res* **2015**, *48* (2), 154–162. https://doi.org/10.1021/ar500237c.

(44) Du, R.; Joswig, J.-O.; Fan, X.; Hübner, R.; Spittel, D.; Hu, Y.; Eychmüller, A. Disturbance-Promoted Unconventional and Rapid Fabrication of Self-Healable Noble Metal Gels for (Photo-)Electrocatalysis. *Matter* **2020**, *2* (4), 908–920. https://doi.org/10.1016/j.matt.2020.01.002.

(45) Du, R.; Wang, J.; Wang, Y.; Hübner, R.; Fan, X.; Senkovska, I.; Hu, Y.; Kaskel, S.; Eychmüller, A. Unveiling Reductant Chemistry in Fabricating Noble Metal Aerogels for Superior Oxygen Evolution and Ethanol Oxidation. https://doi.org/10.1038/s41467-020-15391-w.

(46) Yoon, D.; Bang, S.; Park, J.; Kim, J.; Baik, H.; Yang, H.; Lee, K. One Pot Synthesis of Octahedral {111} CuIr Gradient Alloy Nanocrystals with a Cu-Rich Core and an Ir-Rich Surface and Their Usage as Efficient Water Splitting Catalyst. *CrystEngComm* **2015**, *17* (36), 6843–6847. https://doi.org/10.1039/c5ce00061k.

(47) Pei, J.; Mao, J.; Liang, X.; Chen, C.; Peng, Q.; Wang, D.; Li, Y. Ir–Cu Nanoframes: One-Pot Synthesis and Efficient Electrocatalysts for Oxygen Evolution Reaction. *Chemical Communications* **2016**, *52* (19), 3793–3796. https://doi.org/10.1039/C6CC00552G.

(48) Lim, J.; Yang, S.; Kim, C.; Roh, C.-W.; Kwon, Y.; Kim, Y.-T.; Lee, H. Shaped Ir–Ni Bimetallic Nanoparticles for Minimizing Ir Utilization in Oxygen Evolution Reaction. *Chemical Communications* **2016**, *52* (32), 5641–5644. https://doi.org/10.1039/C6CC00053C.

(49) Park, J.; Sa, Y. J.; Baik, H.; Kwon, T.; Joo, S. H.; Lee, K. Iridium-Based Multimetallic Nanoframe@Nanoframe Structure: An Efficient and Robust Electrocatalyst toward Oxygen Evolution Reaction. *ACS Nano* **2017**, *11* (6), 5500–5509. https://doi.org/10.1021/acsnano.7b00233.

(50) Wang, L. L.; Johnson, D. D. Predicted Trends of Core-Shell Preferences for 132 Late Transition-Metal Binary-Alloy Nanoparticles. *J Am Chem Soc* **2009**, *131* (39), 14023–14029. https://doi.org/10.1021/ja903247x.

(51) González, E.; Arbiol, J.; Puntes, V. F. Carving at the Nanoscale: Sequential Galvanic Exchange and Kirkendall Growth at Room Temperature. *Science (1979)* **2011**, *334* (6061), 1377–1380. https://doi.org/10.1126/science.1212822.

(52) Bang, S.; Yoon, D.; Kim, J.; Baik, H.; Yang, H.; Lee, K. Formation of Double Layer Hollow Nanostars of Pd/CuIr by Utilizing a Kirkendall Effect and a Facile Cu Atom Movement along Twinning Boundaries and Their Usage as Efficient Water Splitting Catalysts. *CrystEngComm* **2015**, *17* (22), 4084–4088. https://doi.org/10.1039/C5CE00538H.

(53) Ren, M.; Chen, J.; Li, Y.; Zhang, H.; Zou, Z.; Li, X.; Yang, H. Lattice Contracted Pd-Hollow Nanocrystals: Synthesis, Structure and Electrocatalysis for Formic Acid Oxidation. *J Power Sources* **2014**, *246*, 32–38. https://doi.org/10.1016/j.jpowsour.2013.07.067.

(54) Nong, H. N.; Gan, L.; Willinger, E.; Teschner, D.; Strasser, P. IrOx Core-Shell Nanocatalysts for Cost- and Energy-Efficient Electrochemical Water Splitting. *Chem. Sci.* **2014**, *5* (8), 2955–2963. https://doi.org/10.1039/C4SC01065E.

(55) Grosvenor, A. P.; Biesinger, M. C.; StC Smart, R.; Stewart McIntyre, N. New Interpretations of XPS Spectra of Nickel Metal and Oxides. **2006**. https://doi.org/10.1016/j.susc.2006.01.041.

(56) Payne, B. P.; Biesinger, M. C.; McIntyre, N. S. The Study of Polycrystalline Nickel Metal Oxidation by Water Vapour. *J Electron Spectros Relat Phenomena* **2009**, *175* (1–3), 55–65. https://doi.org/10.1016/J.ELSPEC.2009.07.006.

(57) Biesinger, M. C.; Payne, B. P.; Lau, L. W. M.; Gerson, A.; Smart, R. St. C. X-Ray Photoelectron Spectroscopic Chemical State Quantification of Mixed Nickel Metal, Oxide and Hydroxide Systems. *Surface and Interface Analysis* **2009**, *41* (4), 324–332. https://doi.org/10.1002/sia.3026.

(58) Reier, T.; Pawolek, Z.; Cherevko, S.; Bruns, M.; Jones, T.; Teschner, D.; Selve, S.; Bergmann, A.; Nong, H. N.; Schlögl, R.; Mayrhofer, K. J. J.; Strasser, P. Molecular Insight in Structure and Activity of Highly Efficient, Low-Ir Ir–Ni Oxide Catalysts for Electrochemical Water Splitting (OER). *J Am Chem Soc* **2015**, *137* (40), 13031–13040. https://doi.org/10.1021/jacs.5b07788.

(59) Tan, X.; Shen, J.; Semagina, N.; Secanell, M. Decoupling Structure-Sensitive Deactivation Mechanisms of Ir/IrOx Electrocatalysts toward Oxygen Evolution Reaction. *J Catal* **2019**, *371*, 57–70. https://doi.org/10.1016/j.jcat.2019.01.018.

(60) Alia, S. M.; Shulda, S.; Ngo, C.; Pylypenko, S.; Pivovar, B. S. Iridium-Based Nanowires as Highly Active, Oxygen Evolution Reaction Electrocatalysts. *ACS Catal* **2018**, *8* (3), 2111–2120. https://doi.org/10.1021/acscatal.7b03787.

(61) Godínez-Salomón, F.; Albiter, L.; Alia, S. M.; Pivovar, B. S.; Camacho-Forero, L. E.; Balbuena, P. B.; Mendoza-Cruz, R.; Arellano-Jimenez, M. J.; Rhodes, C. P. Self-Supported Hydrous Iridium–Nickel Oxide Two-Dimensional Nanoframes for High Activity Oxygen Evolution Electrocatalysts. *ACS Catal* **2018**, *8* (11), 10498–10520. https://doi.org/10.1021/acscatal.8b02171.

(62) Hegge, F.; Lombeck, F.; Cruz Ortiz, E.; Bohn, L.; Von Holst, M.; Kroschel, M.; Hübner, J.; Breitwieser, M.; Strasser, P.; Vierrath, S. Efficient and Stable Low Iridium Loaded Anodes for PEM Water Electrolysis Made Possible by Nanofiber Interlayers. *ACS Appl Energy Mater* **2020**, *3* (9), 8276–8284. https://doi.org/10.1021/acsaem.0c00735.

(63) Antolini, E. Iridium As Catalyst and Cocatalyst for Oxygen Evolution/Reduction in Acidic Polymer Electrolyte Membrane Electrolyzers and Fuel Cells. *ACS Catal* **2014**, *4* (5), 1426–1440. https://doi.org/10.1021/cs4011875.

(64) Li, G.; Li, S.; Xiao, M.; Ge, J.; Liu, C.; Xing, W. Nanoporous IrO 2 Catalyst with Enhanced Activity and Durability for Water Oxidation Owing to Its Micro/Mesoporous Structure. *Nanoscale* **2017**, *9* (27), 9291–9298. https://doi.org/10.1039/C7NR02899G.

(65) Oh, H.-S.; Nong, H. N.; Reier, T.; Gliech, M.; Strasser, P. Oxide-Supported Ir Nanodendrites with High Activity and Durability for the Oxygen Evolution Reaction in Acid PEM Water Electrolyzers. *Chem Sci* **2015**, *6* (6), 3321–3328. https://doi.org/10.1039/C5SC00518C.

(66) Oh, H. S.; Nong, H. N.; Reier, T.; Bergmann, A.; Gliech, M.; Ferreira De Araújo, J.; Willinger, E.; Schlögl, R.; Teschner, D.; Strasser, P. Electrochemical Catalyst-Support Effects and Their Stabilizing Role for IrOx Nanoparticle Catalysts during the Oxygen Evolution Reaction. *J Am Chem Soc* **2016**, *138* (38), 12552–12563. https://doi.org/10.1021/jacs.6b07199.

(67) Bender, G.; Carmo, M.; Smolinka, T.; Gago, A.; Danilovic, N.; Mueller, M.; Ganci, F.; Fallisch, A.; Lettenmeier, P.; Friedrich, K. A.; Ayers, K.; Pivovar, B.; Mergel, J.; Stolten, D. Initial Approaches in Benchmarking and Round Robin Testing for Proton Exchange Membrane Water Electrolyzers. *Int J Hydrogen Energy* **2019**, *44* (18), 9174–9187. https://doi.org/10.1016/j.ijhydene.2019.02.074.

(68) Bühler, M.; Hegge, F.; Holzapfel, P.; Bierling, M.; Suermann, M.; Vierrath, S.; Thiele, S. Optimization of Anodic Porous Transport Electrodes for Proton Exchange Membrane Water Electrolyzers. *J Mater Chem A Mater* **2019**, *7* (47), 26984–26995. https://doi.org/10.1039/c9ta08396k.

(69) Audichon, T.; Mayousse, E.; Morisset, S.; Morais, C.; Comminges, C.; Napporn, T. W.; Kokoh, K. B. Electroactivity of RuO2-IrO2 Mixed Nanocatalysts toward the Oxygen Evolution Reaction in a Water Electrolyzer Supplied by a Solar Profile. *Int J Hydrogen Energy* **2014**, *39* (30), 16785–16796. https://doi.org/10.1016/j.ijhydene.2014.07.170.

(70) Alia, S. M.; Rasimick, B.; Ngo, C.; Neyerlin, K. C.; Kocha, S. S.; Pylypenko, S.; Xu, H.; Pivovar, B. S. Activity and Durability of Iridium Nanoparticles in the Oxygen Evolution Reaction. *J Electrochem Soc* **2016**, *163* (11), F3105–F3112. https://doi.org/10.1149/2.0151611jes.

(71) Zhao, S.; Stocks, A.; Rasimick, B.; More, K.; Xu, H. Highly Active, Durable Dispersed Iridium Nanocatalysts for PEM Water Electrolyzers. *J Electrochem Soc* **2018**, *165* (2), F82–F89. https://doi.org/10.1149/2.0981802JES/XML.

(72) Jovanovič, P.; Hodnik, N.; Ruiz-Zepeda, F.; Arčon, I.; Jozinović, B.; Zorko, M.; Bele, M.; Šala, M.; Šelih, V. S.; Hočevar, S.; Gaberšček, M. Electrochemical Dissolution of Iridium and Iridium Oxide Particles in Acidic Media: Transmission Electron Microscopy, Electrochemical Flow Cell Coupled to Inductively Coupled Plasma Mass Spectrometry, and X-Ray Absorption Spectroscopy Study. *J Am Chem Soc* **2017**, *139* (36), 12837–12846. https://doi.org/10.1021/JACS.7B08071/SUPPL_FILE/JA7B08071_SI_001.PDF.

(73) Geiger, S.; Kasian, O.; Shrestha, B. R.; Mingers, A. M.; Mayrhofer, K. J. J.; Cherevko, S. Activity and Stability of Electrochemically and Thermally Treated Iridium for the Oxygen Evolution Reaction. *J Electrochem Soc* **2016**, *163* (11), F3132–F3138. https://doi.org/10.1149/2.0181611JES/XML.

(74) Cherevko, S.; Reier, T.; Zeradjanin, A. R.; Pawolek, Z.; Strasser, P.; Mayrhofer, K. J. J. Stability of Nanostructured Iridium Oxide Electrocatalysts during Oxygen Evolution Reaction in Acidic Environment. *Electrochem commun* **2014**, *48*, 81–85. https://doi.org/10.1016/J.ELECOM.2014.08.027.

(75) Alia, S. M.; Ha, M.-A.; Anderson, G. C.; Ngo, C.; Pylypenko, S.; Larsen, R. E. The Roles of Oxide Growth and Sub-Surface Facets in Oxygen Evolution Activity of Iridium and Its Impact on Electrolysis. *J Electrochem Soc* **2019**, *166* (15), F1243–F1252. https://doi.org/10.1149/2.0771915jes.

(76) Park, S.; Shviro, M.; Hartmann, H.; Mayer, J.; Carmo, M.; Stolten, D. Cation-Exchange Method Enables Uniform Iridium Oxide Nanospheres for Oxygen Evolution Reaction. *ACS Appl Nano Mater* **2022**, *5* (3), 4062–4071. https://doi.org/10.1021/ACSANM.2C00031/ASSET/IMAGES/LARGE/AN2C00031_0006.JPEG.

(77) Pfeifer, V.; Jones, T. E.; Velasco Vélez, J. J.; Massué, C.; Arrigo, R.; Teschner, D.; Girgsdies, F.; Scherzer, M.; Greiner, M. T.; Allan, J.; Hashagen, M.; Weinberg, G.; Piccinin, S.; Hävecker, M.; Knop-Gericke, A.; Schlögl, R. The Electronic Structure of Iridium and Its Oxides. *Surface and Interface Analysis* **2016**, *48* (5), 261–273. https://doi.org/10.1002/sia.5895.

(78) Xu, S.; Chen, S.; Tian, L.; Xia, Q.; Hu, W. Selective-Leaching Method to Fabricate an Ir Surface-Enriched Ir-Ni Oxide Electrocatalyst for Water Oxidation. *Journal of Solid State Electrochemistry* **2016**, *20* (7), 1961–1970. https://doi.org/10.1007/s10008-016-3200-0.

(79) Pfeifer, V.; Jones, T. E.; Velasco Vélez, J. J.; Massué, C.; Greiner, M. T.; Arrigo, R.; Teschner, D.; Girgsdies, F.; Scherzer, M.; Allan, J.; Hashagen, M.; Weinberg, G.; Piccinin, S.; Hävecker, M.; Knop-Gericke, A.; Schlögl, R. The Electronic Structure of Iridium Oxide Electrodes Active in Water Splitting. *Physical Chemistry Chemical Physics* **2016**, *18* (4), 2292–2296. https://doi.org/10.1039/c5cp06997a.

(80) Moulder, J. F.; Stickle, W. F.; Sobol, P. E. ′; Bomben, K. D.; Chastain, J. Handbook of X-Ray Photoelectron Spectroscopy AReference Book of Standard Spectra for Identification and Interpretation of XPS Data.

(81) Siracusano, S.; Baglio, V.; Grigoriev, S. A.; Merlo, L.; Fateev, V. N.; Aricò, A. S. The Influence of Iridium Chemical Oxidation State on the Performance and Durability of Oxygen Evolution Catalysts in PEM Electrolysis. *J Power Sources* **2017**, *366*, 105–114. https://doi.org/10.1016/J.JPOWSOUR.2017.09.020.

TOC

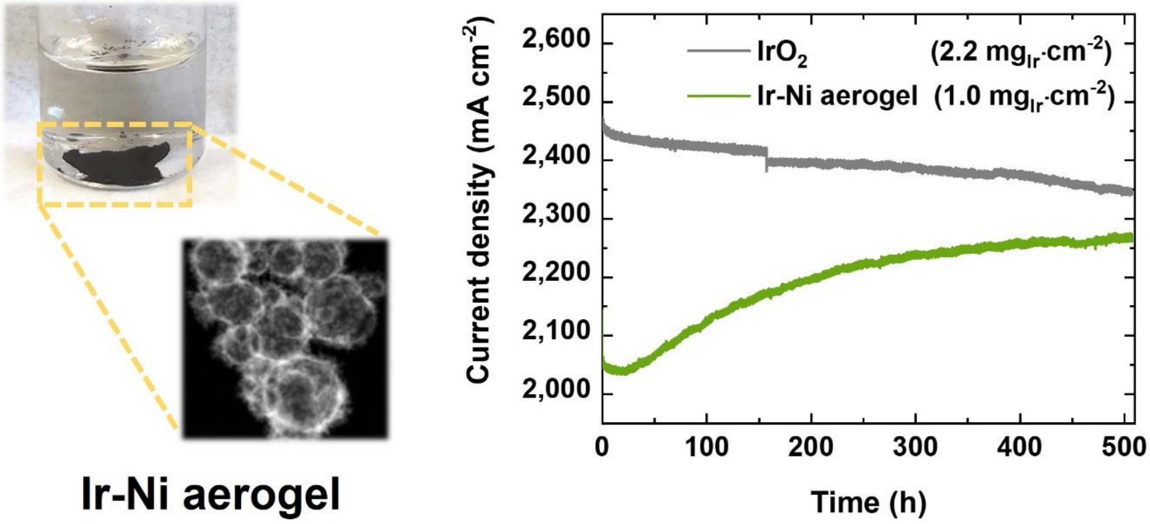
Ir-Ni aerogel
Current density (mA cm^{-2})
2,000
2,100
2,200
2,300
2,400
2,500
2,600
Time (h)
0
100
200
300
400
500
IrO$_2$ (2.2 mg$_{Ir}$·cm^{-2})
Ir-Ni aerogel (1.0 mg$_{Ir}$·cm^{-2})